Indirect excitation and luminescence activation of Tb doped indium tin oxide and its impact on the host's optical and electrical properties

P. Llontop[1,†], C. E. Torres[1], M. Piñeiro[1], L. Conde[1], A. Tejada[1,2], J. A. Töfflinger[1], F. Rumiche[3], F. F. H. Aragón[4], D. G. Pacheco-Salazar[4], R. Grieseler[1], L. Korte[2], and J. A. Guerra[1,‡]

[1]Departamento de Ciencias, Sección Física, Pontificia Universidad Católica del Perú, Av. Universitaria 1801, 15088, Lima, Perú
[2]Helmholtz-Zentrum Berlin für Materialien und Energie GmbH, Young Investigator Group for Perovskite Tandem Solar Cells, Kekuléstraβe 5, 12489 Berlin, Germany
[3]Departamento de Ingeniería, Sección Mecánica, Pontificia Universidad Católica del Perú, Av. Universitaria 1801, 15088, Lima, Perú
[4]Laboratorio de Películas Delgadas, Escuela Profesional de Física, Universidad Nacional de San Agustín de Arequipa, Av. Independencia, Arequipa, Perú

E-mail: [†]p.llontop@pucp.edu.pe and [‡]guerra.jorgea@pucp.edu.pe

Abstract.

The effect of terbium doping on the electrical, optical and light emission properties of sputtered indium tin oxide thin films was investigated. The films were prepared by radio frequency dual magnetron sputtering, maintaining a high optical transmittance in the ultraviolet and visible spectral regions, and a low electrical resistivity ranging from $5 \times 10^{-3}\,\Omega \cdot \mathrm{cm}$ to $0.3\,\Omega \cdot \mathrm{cm}$. Terbium-related luminescence is achieved after annealing at 470 °C in air at atmospheric pressure. Electrical resistivity and optical transmittance were measured after each annealing step to evaluate the compromise between the achieved light emission intensity, electrical and optical properties. Additionally, temperature dependence of Tb-related luminescence quenching was assessed by temperature-dependent photoluminescence measurements, from 83 K to 533 K, under non-resonant excitation. Thermal quenching activation energies suggest an effective energy transfer mechanism from the ITO host to the rare-earth ions. This indirect excitation mechanism was modeled using a spherical potential-well and a tight-binding one-band approximation approaches, describing a short-range charge trapping process and subsequent formation of bound excitons to rare-earth ion clusters.

Submitted to: *J. Phys. D: Appl. Phys.*

1. Introduction

Rare-earth (RE) doped wide bandgap semiconductors have attracted great attention as efficient luminescent materials for optoelectronic applications, like photon downshift, as well as down- and up-conversion systems [1, 2], optical amplifiers [3, 4], electroluminescent devices [5, 6], lasers [7, 8], non-contact luminescent temperature sensors [9–11], and photonic structures [12–14]. Recently, RE based down- and up-conversion layers have been effectively integrated in solar cells [15–17]. This is attributed to two principal features. First, a large bandgap suppresses the thermal quenching effect at room temperature and, in some cases, even at higher temperatures. This allows RE-related light emission output, for instance, in the visible spectral range covering the colors red (Eu^{3+}), green (Tb^{3+}) and blue (Tm^{3+}) [18–20]. Second, RE-related light emission exhibits long fluorescence lifetimes and narrow spectra, since they result from intra-4f electronic transitions, which are weakly sensitive to the host atomic environment [21–23]. Furthermore, the host's semiconducting properties allow the tailoring of the electrical properties of the material without dramatically compromising its optical properties and light emission capabilities.

These features make RE doped wide bandgap semiconductors suitable for light emission applications, as an alternative to direct semiconductor based devices [5, 6], and light conversion applications which can be integrated in solar cells [15–17]. However, the RE-related light emission intensity is sensitive to the host environment, oxygen content, disorder-induced states and other localized electronic states [5, 20–28]. In particular, it is well established that not all the REs embedded in a host are active for light emission, but can be activated through post-deposition thermal treatments [20–23, 28]. These treatments have two effects that may enhance the RE-related light emission intensity. First, annealing may induce the coordination of RE ions with neighboring host ions in a non-centrosymmetric arrangement, thus enhancing the probability of intra-4f electronic transitions. Second, electronic defects such as dangling bonds may also play an important role in energy transfer mechanisms from the host to RE ions. In general, the density of localized states and host related luminescent centers can be thermally enhanced or quenched, affecting the overall RE light emission output [21–29].

In this context, little is known about the light emission features of RE-doped transparent conductive oxides (TCOs), like for instance indium tin oxide (ITO) or aluminum doped zinc oxide (AZO), among others. Functional light emitting materials like RE doped TCOs could open applications, for instance, in low voltage direct current electroluminescent devices, or energy-downshift transparent, anti-reflective, and electrically conductive layers. In contrast to traditional wide bandgap semiconductors, the electrical conductivity could be high enough to still use the material as a transparent and luminescent electric contact. However, there are only very few and recent published works where ITO or AZO have been doped with REs, and very low or no light emission intensity has been achieved in these systems [26, 30–32]. To the best of our knowledge, to date there is no published report on Tb-related light emission from Tb^{3+} doped ITO or AZO. In contrast, there are reports on the light emission of RE-doped zinc oxide (ZnO) [33, 34], aluminum oxide (Al_2O_3) [35], indium oxide (In_2O_3) [36, 37], and tin oxide (SnO_2) [38, 39]. These materials exhibit an optical transparency suitable for light output from luminescent centers, and a wide bandgap capable of overcoming the thermal quenching effect at room temperature. Their optical and electrical properties can be engineered for instance by tailoring the oxygen content during the deposition process or by post-deposition annealing treatments, reducing or increasing in this way the amount of oxygen vacancies, thus reducing (increasing) the electrical conductivity whilst increasing (reducing) its transparency [40]. We believe that the absence of Tb emission in previous reports from these ternary compounds is related to an effective competition between host related recombination centers and radiative recombination involving the REs, in addition to an inhibited thermal activation of the REs due to the absence of a proper crystal symmetry surrounding them.

In this work, we aim to shed some light on the capability of RE doped TCOs to become optically active, while retaining important properties of the host material such as a low resistivity and high optical transmittance in the visible spectral region. We present the synthesis and characterization of Tb^{3+} doped ITO thin films grown by RF magnetron sputtering. Our approach consists of growing the films while actively cooling the substrates during the deposition process, and subsequently promoting the

thermally-induced rearrangement of Tb ions to a more suitable position by means of post-deposition thermal treatments. Previous attempts have shown that, when the films are not grown with active cooling, there is no Tb activation in the annealing temperature range from 200 °C to 1000 °C. Here, efficient Tb-related light emission is obtained under non-resonant ultraviolet photon excitation after annealing at 470 °C. The effect of Tb^{3+} doping on the optical and electrical properties is assessed for different annealing temperatures. Finally, the excitation mechanism is probed by temperature-dependent photoluminescence measurements, and tentatively modeled by a short-range charge trapping process and the formation of excitons bound to RE ion clusters. From this model, the exciton binding energies are calculated.

2. Experimental details

ITO and Tb^{3+} doped ITO thin films were grown on two-side polished silicon and fused silica substrates by RF magnetron sputtering using ITO (4N) and Tb (3N) targets with a diameter of 2 inches. The ITO target used was 90 wt.% indium oxide (In_2O_3) and 10 wt.% tin oxide (SnO_2). The targets were mounted facing the substrate holder, aiming towards the same spot, thus obtaining different Tb concentrations simultaneously throughout several laterally separated substrates in a single process. The distance between the targets and substrate was fixed at 7.5 cm. The substrates were cleaned in an ultrasonic bath using acetone for 10 minutes and deionized water afterwards. The deposition process was carried out under a 30 sccm argon flow. The base pressure of the sputtering chamber was below 4.0×10^{-6} mbar prior to the deposition and the working pressure was fixed at 1.0×10^{-2} mbar. Targets were sputtered simultaneously with a power of 100 W and 10 W for ITO and Tb, respectively. The deposition process lasted five hours and film thickness ranged from 300 nm to 500 nm. To allow the luminescence activation by post-deposition annealing, the samples were mounted to an actively cooled sample holder with a closed-cycle water cooling system set to 15 °C. In this way the sample is grown with a lower crystallinity or even an amorphous phase. After deposition, samples were annealed from 150 °C to 650 °C for 3 hours in air atmosphere. Same sample for each annealing step. An undoped ITO thin film was used as a reference sample and annealed to also evaluate the effect of the annealing and inclusion of Tb ions on the electrical and optical properties of the undoped host material under similar growth conditions.

Elemental composition measurements were performed by energy dispersive X-ray spectroscopy (EDX), employing a FEI Quanta 650 scanning electron microscope (SEM) equipped with a tungsten filament and a concentric backscattered electron detector. Electrons were accelerated with a relatively low applied voltage of 6.5 kV in order to reduce the silicon signal contribution from the substrate. Measurements were performed three times near the middle of each sample on a ×200 magnification and then averaged. The quantification was made with EDAX's TEAM EDS analysis system, employing the ZAF correction procedure [41]. Figure 1 shows the element concentration versus the Tb concentration of the as-grown (AG) samples and after annealing treatments for an undoped ITO film and a 0.86 at.% Tb doped ITO film.

X-ray diffraction (XRD) measurements were carried out using a Bruker D8 Discover in grazing incidence configuration. The as-grown samples

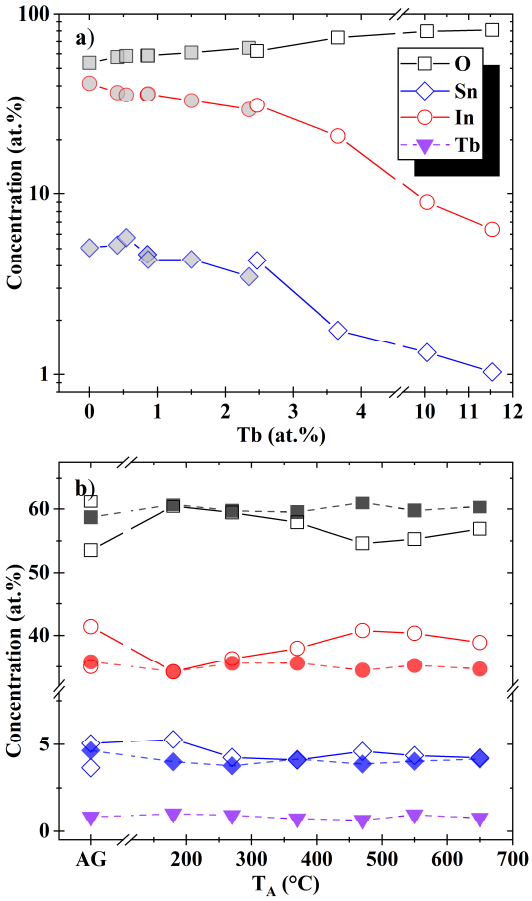

Figure 1: Atomic concentration of as grown Tb doped ITO thin films deposited on silicon (open symbols) and fused silica (filled symbols) substrates, as obtained from EDS (a). Atomic concentration of an undoped ITO (open symbols) and 0.86 at.% Tb doped ITO (solid symbols) films versus annealing temperature (b).

exhibited a mixed polycrystalline and amorphous structure, induced by the active cooling and Tb doping during the deposition process. Full crystallization is achieved after annealing at 550 °C. Figure 2 depicts diffraction patterns of the as-grown and 550 °C annealed samples for the undoped and 0.86 at.% Tb doped cases. Note how the presence of Tb ions in the host induce the amorphous state before thermal treatments. After annealing, crystallization takes place, however it can be inferred from the width of the peaks that the grain size is smaller in the Tb doped case. Table 1 summarizes the crystal size and lattice strain obtained by a Rietveld analysis from the diffractograms depicted in Fig. 2.

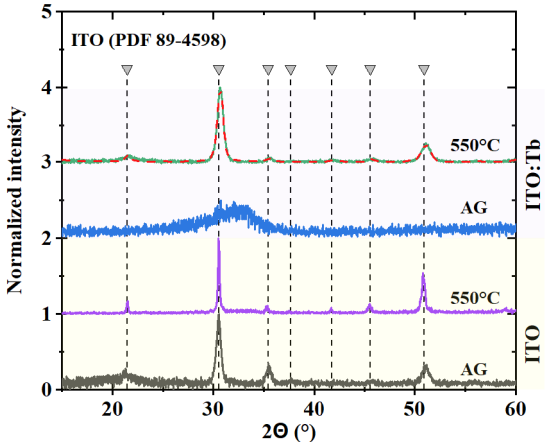

Figure 2: X-ray diffraction patterns of the ITO and 0.86 at.% Tb doped ITO samples before and after annealing at 550 °C. PDF peaks positions of ITO are also plotted. The corresponding crystal size and lattice strain calculated after a Rietveld analysis are summarized in table 1. Diffractograms were normalized and shifted for better visibility.

Optical transmittance measurements were performed using a Perkin Elmer Lambda 950 double beam UV-Vis spectrophotometer, with a spot size of 5 mm diameter and in the spectral range from 250 nm to 2200 nm in steps of 1 nm. Two analyses were performed with these spectra. First, in the spectral region from 250 nm to 850 nm, refractive index, absorption coefficient and thickness were calculated by means of a modified envelope method optimized for the determination of the fundamental absorption and implemented in a Wolfram Mathematica script [42]. This information was then used to determine the optical bandgap accurately. Fig. 3 shows the optical transmittance, refractive index and absorption coefficient of four different ITO samples with 0, 1.5, 2.3 and 3.7 at.% Tb along with the mentioned fits and corresponding thicknesses.

Second, a full spectrum analysis using Drude and Tauc-Lorentz oscillators was performed to determine

Table 1: Crystal size and lattice strain of the undoped ITO and 0.86 at.% Tb doped ITO layers, before and after annealing treatments at 550 °C. The values were obtained from a Rietveld analysis of the diffractograms depicted in figure 2. Retrieved lattice parameters are 10.093(4) Å and 10.092(3) Å for the AG and 550 °C annealed ITO, respectively, and 10.095(2) Å for the Tb doped ITO annealed at 550 °C.

	Crystal size (nm)		Lattice strain (%)	
Sample	AG	550 °C	AG	550 °C
ITO	36.5(55)	59.1(77)	1.41(6)	0.54(3)
ITO:Tb^{3+}	-	21.0(9)	-	1.82(3)

the charge carrier density and mobility by means of the software SpectraRay from SENTECH Instruments. In this case, the optical system had to be modeled as two layers with different Drude parameters but same Tauc-Lorentz parameters, the reason being the low penetration depth in the spectral region where the Tauc-Lorentz oscillator has the highest absorption [43, 44]. The top layer exhibited a larger free carrier absorption than the bottom one, and in most cases the bottom layer didn't exhibit free carrier absorption at all. Figs. 4 and 5 depict the transmittance fits for the undoped reference ITO film and the 2.3 at.% Tb doped ITO film, for different annealing temperatures and their corresponding calculated Drude parameters.

Photoluminescence (PL) measurements were performed in a back reflection geometry using a Renishaw micro Raman inVia spectrometer. The excitation wavelength was 325 nm from an He-Cd laser with an average power excitation density of $\sim$1.5 W/m^2. The laser spot was focused on the sample surface for each measurement. Measurements were taken on Tb doped and undoped ITO samples grown on silicon substrates. Sample temperature was controlled by means of a Linkam cooling stage with a liquid nitrogen inlet. Cathodoluminescence (CL) measurements were carried out using a Horiba HCL-I312 spectrometer equipped with a parabolic mirror attached to the SEM under a 5 kV electron beam acceleration voltage.

Resistivity measurements were performed at room temperature using a four point system by employing the van der Pauw technique on square-shaped samples (10 mm × 10 mm) grown on fused silica. A Keithley 2450 source measure unit (SMU) was used as the current source and voltmeter. A Keithley 7709 matrix module was employed for the switching configuration. Gold coated spring tips were used to make electrical contact with the films. Uniform pressure on all four contacts was assessed by means of current-voltage measurements, in which all samples showed an ohmic behaviour.

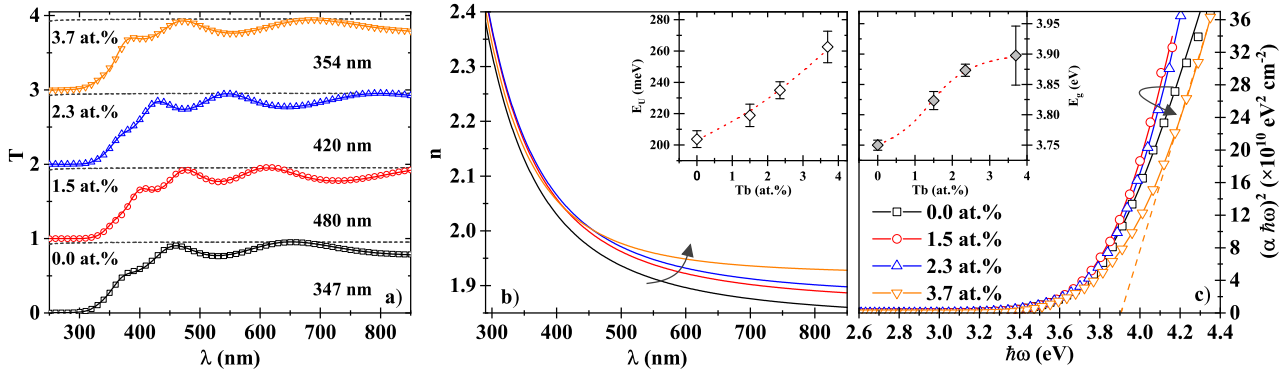

Figure 3: Optical transmittance of as-grown Tb doped ITO thin films grown on fused silica substrates for different Tb concentrations alongside the substrate transmittance (dashed gray lines). Solid lines are fits using a modified Swanepoel method [42]. The corresponding thickness and doping concentration are denoted in nm and at.%, respectively (a). Refractive index (b) and absorption coefficient (c) calculated from the optical transmittance measurements. The absorption coefficient is plotted in the $(\alpha\hbar\omega)^2$ scale. Solid curves are fits using a band-fluctuations model for direct semiconductors, Eq. (1). The dashed line highlights the linear behaviour of the fundamental absorption in this scale, which is the behaviour expected from theory for a direct semiconductor [45]. Note that only 60 data points out of 600 are plotted to avoid visual clutter. Dotted lines in inset graphs are a guide to the eye.

3. Results and discussion

In this section we summarize the results of the effects of Tb doping and subsequent activation by post-deposition thermal treatments, on the optical, electrical and light emission properties of sputtered ITO thin films. The light emission intensity versus sample temperature is presented. From this, two activation energies associated to the thermal quenching process are determined. The underlying excitation mechanism and thermal quenching process are assessed by means of a spherical potential-well and Koster-Slater trap models [46, 47], in order to describe the possible indirect excitation mechanism of Tb ions by means of the formation of bound excitons.

3.1. Optical properties

Figure 3 depicts the optical transmittance and the corresponding retrieved refractive index $n(\lambda)$ versus photon wavelength λ, and absorption coefficient $\alpha(\hbar\omega)$ versus photon energy $\hbar\omega$, of the as grown ITO:Tb^{3+} films for different Tb concentrations, covering the fundamental absorption and transparent spectral regions. All samples exhibited a high optical transmittance in the visible spectrum, independently of the Tb content or annealing temperature. A systematic increase of n with increasing Tb concentration is observed, in agreement with the effect of oxygen in the refractive index and material densification [48], whereas the variation of the fundamental absorption is tracked by changes in the optical bandgap (E_g) and Urbach energy (E_U), depicted in the inset graphs of Fig. 3. The latter parameters are determined by fitting the absorption coefficient with a fundamental absorption model for direct semiconductors. We use a band-fluctuations model for direct materials [49],

$$\alpha(\hbar\omega) = -\frac{1}{2}\frac{\alpha_0}{\hbar\omega}\sqrt{\frac{\pi}{\beta}}\mathrm{Li}_{1/2}\left(-\mathrm{e}^{\beta(\hbar\omega - E_g)}\right). \qquad (1)$$

Here $\mathrm{Li}_{1/2}(z)$ is the polylogarithm function of order $1/2$ of z. β is the Urbach slope (reciprocal of E_U), and α_0 is a coefficient proportional to the electronic transition matrix element.

Table 2: Optical bandgap E_g retrieved with Eq. (1), fundamental $(\alpha\hbar\omega)^2$-gap and Urbach energy E_U of ITO with different Tb concentrations.

Tb (at.%)	E_g (eV)	$(\alpha\hbar\omega)^2$ (eV)	E_U (meV)
0	3.75(8)	3.73(3)	203.7(53)
1.5	3.82(14)	3.80(9)	218.8(71)
2.3	3.87(10)	3.85(7)	234.9(53)
3.7	3.89(48)	3.84(4)	262.5(100)

The advantage of using the model yielding Eq. (1), for retrieving the optical bandgap and Urbach energy, lies on the fact that materials with large Urbach tails will exhibit a bias on the bandgap when using

traditional models. This is due to the large overlap of the Urbach tail with the fundamental absorption onset. Typically, for values of E_U above 60 meV, a significant deviation between the actual bandgap and the retrieved E_g is found [28, 49–52]. Since Eq. (1) takes into account Urbach tails, the retrieved bandgap is typically free of this bias [49]. Table 2 summarizes the Urbach energies and bandgaps calculated by fitting Eq. (1) to the absorption coefficient. Additionally, the $(\alpha\hbar\omega)^2$-gap assumed for direct semiconductors is also listed [45].

Here, the increment of E_g and E_U observed with increasing Tb concentration is most probably associated to the induced lattice distortion by the presence of Tb ions in the ITO host, the formation of charged defects, and presence of suboxide species. Tb ions disrupt the lattice, thus inducing strain, inhibiting the formation of larger grains during deposition and inducing the formation of oxygen vacancies, all of which lead to a larger Urbach energy. Since Tb inclusion promotes the formation of charged vacancies when disrupting the lattice [53–55], we could expect an optical bandgap shift attributed to the Burstein-Moss effect. Nevertheless, the formation of Tb suboxides could also play a role in the bandgap widening. XRD patterns depicted in Fig. 2 and lattice strain shown in Table 1 confirm the Tb-induced lattice distortion. A similar distortion has also been reported for Cu doped non-crystalline SnO_2 [56], and Nd, Eu and Tb doped In_2O_3 sol gel films [26].

Both Tb doped and undoped ITO layers exhibited an increase in the infrared absorption as well as an increase of E_g and E_U with increasing annealing temperature. Both features are related to a annealing-induced increase in the charge carrier density, see Figs. 4, 5 and 6. It has been shown that thermal treatments up to 350 °C increase the electrical conductivity of ITO layers when performed either in inert or reactive atmospheres [40, 57–59]. Nevertheless, for temperatures above 350 °C, electrical conductivity drops depending on the annealing atmosphere used [59]. The reason behind this behaviour is a competition between the thermally-induced activation/deactivation of charged defects along with a variation in the electronic mobility, affecting the electrical conductivity. Typically, for annealing temperatures below 350 °C, Sn ions change their oxidation state from Sn^{2+} to Sn^{4+}, thus acting as donors when occupying In^{3+} sites [59, 60]. On the other hand, annealing treatments in an air atmosphere induce oxygen diffusion into the ITO matrix, therefore reducing the amount of charged oxygen vacancies. This diffusion usually increases the oxygen concentration near the surface of the ITO layer [40]. However, the extent of this diffusion will depend on the available sites or vacancies for oxygen to bond in. That is, for nearly saturated samples, oxygen diffusion from the atmosphere will require more energy than in non-saturated ones to diffuse into. Here, EDX analysis depicted in Fig. 1 showed no major variation of the oxygen content in Tb doped ITO upon annealing. Whilst, for undoped ITO, oxygen reaches the saturation value after the first annealing treatment at 180 °C, from 53.5 at.% to 60.5 at.%, in agreement with previous reports on samples grown in a similar fashion [40].

In order to assess and discern the impact of annealing treatments on the charge carrier density and mobility, we describe the complex refractive index $\tilde{n}$ by a combination of Tauc-Lorentz and Drude-Lorentz models depicted in Eq. 2, and fit the optical transmittance of ITO and ITO:Tb for each annealing temperature.

$$\tilde{n}^2 = \varepsilon_1 + i\varepsilon_2 = \varepsilon_1(\infty) - \frac{\omega_p^2}{\nu^2 + i\omega_\tau \nu} + \sum_l \frac{\Omega_{p,l}}{\Omega_{0,l}^2 - \nu^2 - i\Omega_{\tau,l}\nu} + \sum_l {}^{\mathrm{TL}}\tilde{\varepsilon}_l \quad (2)$$

with

$$\mathrm{Im}({}^{\mathrm{TL}}\tilde{\varepsilon}_l) = \frac{A_l E_{0,l} C_l (E - E_{g,l})^2}{(E^2 - E_{0,l}^2)^2 + C_l^2 E^2} \frac{1}{E} \Theta(E - E_{g,l})$$

Here, ε_1 and ε_2 are the real and imaginary part of the complex dielectric function $\tilde{\varepsilon}$, respectively. ν and E are the photon wavenumber and photon energy, respectively. $\tilde{n}$ is the complex refractive index. ${}^{\mathrm{TL}}\tilde{\varepsilon}_l$ is the Tauc-Lorentz dielectric function contribution, from which the real part is obtain by a Kramers-Kronig transformation [61]. Θ is a Heavyside function.

The fitting parameteres in this expression are the Tauc-Lorentz oscillator strength A_l, peak central energy $E_{0,l}$, broadening parameter C_l, Lorentz oscillator strength $\Omega_{p,l}$, frequency center $\Omega_{0,l}$ and damping $\Omega_{\tau,l}$, and Drude plasma frequency ω_p and collision frequency ω_τ. The last two being related to the charge carrier density N and mobility μ by

$$\omega_p = \sqrt{\frac{Ne^2}{\varepsilon_0 m_e^*}} \quad (3)$$

and

$$\omega_\tau = \frac{e}{\mu m_e^*}, \quad (4)$$

with ε_0, e and m_e^* the vacuum permittivity, elemental charge and electron effective mass, respectively.

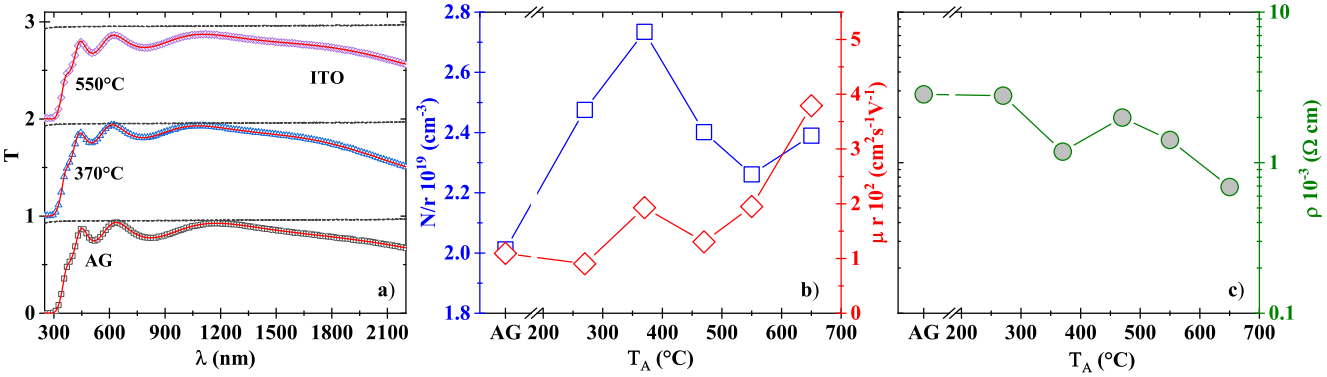

Figure 4: Optical transmittance (a), charge carrier and mobility (b) and electrical resistivity (c) of ITO thin films versus annealing temperature, as determined from the Drude model. r denotes the ratio between the electron effective mass and the electron rest mass.

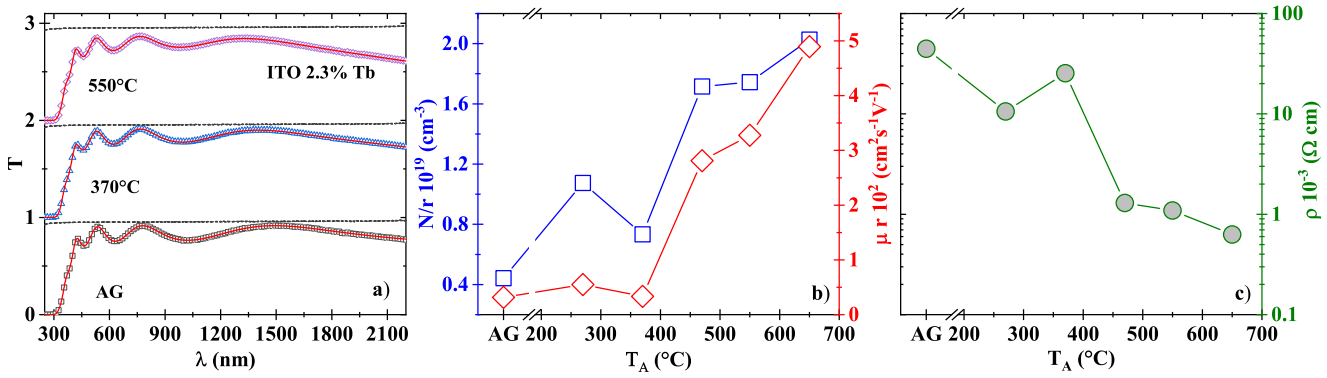

Figure 5: Optical transmittance (a), charge carrier and mobility (b) and electrical resistivity (c) of 2.3 at.% Tb doped ITO thin films versus annealing temperature, as determined from the Drude model. r denotes the ratio between the electron effective mass and the electron rest mass.

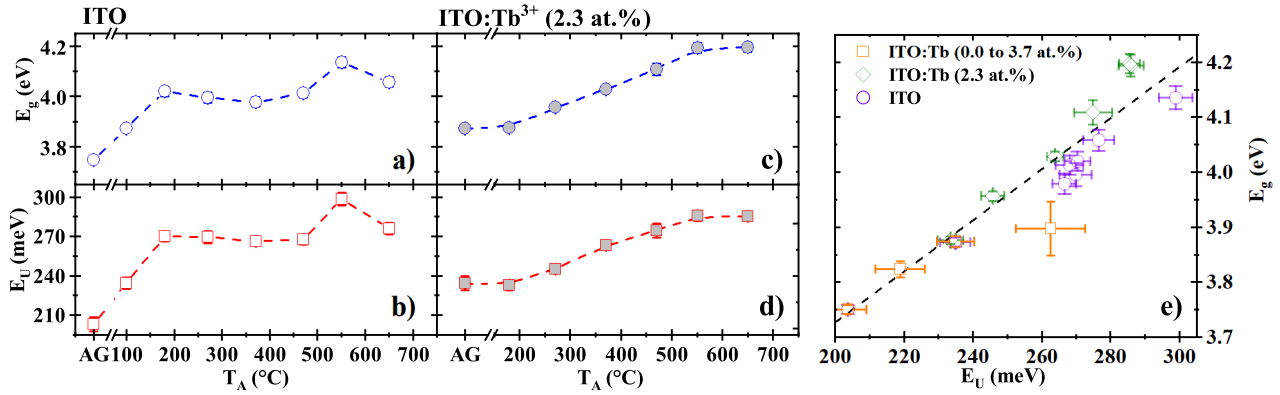

Figure 6: Optical bandgap and Urbach energy versus annealing temperature for the undoped (a)(b) and Tb doped (c)(d) ITO layers. Optical bandgap versus Urbach energy for different annealing treatments and Tb concentrations (e).

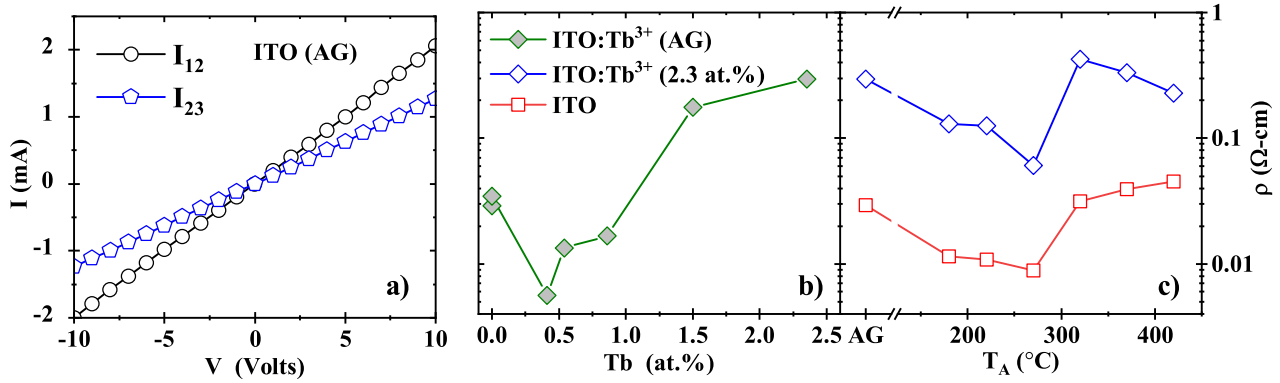

Figure 7: Current-voltage curves of an as grown (AG) ITO sample for two permutations passing the current trough the contacts 1 and 2, and then by the contacts 2 and 3 (a). Electrical resistivity versus Tb atomic concentration without thermal treatments (b). Electrical resistivity versus annealing temperature for the undoped and Tb doped cases (c).

Sample layers had to be modeled as a two-film stack with the same Tauc-Lorentz and Lorentz oscillators parameters, but distinct Drude parameters. This is due to the growth-induced microstructure sputtered ITO thin films typically exhibit and the low penetration depth in the high absorption spectral region where Tauc-Lorentz has the most influence [43, 44, 53, 62–65]. The first layer, or bottom layer, exhibits poor electrical properties, whereas the top layer is more conductive. In most cases, the optical transmittance fit is achieved by three Tauc-Lorentz oscillators and one Lorentz oscillator.

We focus here on the Drude parameters of the top layer. Figs. 4 and 5 depict the infrared analysis on the optical transmittance of ITO and 2.3 at.% Tb doped ITO films for different annealing treatments, respectively. N and μ are calculated from ω_p and ω_τ in terms of the electron effective mass m_e^*. In these systems, m_e^* is a fraction r of the rest mass of an electron $m_e^* = rm_e$, which is typically around $r \sim 0.35$ [66]. Two features are noted in these figures. First, Tb doped ITO has a higher resitivity than the undoped ITO films. The charge carrier density of Tb doped ITO is significantly lower than undoped ITO. Tb ions might be replacing Sn and/or In ions, inhibiting the formation of Sn^{4+} and thus limiting the charge carrier density. Additionally, for annealing temperatures below 400 °C, the electron mobility is also smaller due to the induced lattice distortion. Second, the charge carrier density of the undoped ITO sample exhibits a maximum value after 370 °C annealing and drops for higher annealing temperatures. This effect is in agreement with the formation of Sn^{4+} for lower annealing temperatures. The observed drop of N for higher temperatures would be associated to oxygen diffusion into the film occupying vacancies and the formation of Sn-O complexes deactivating donor Sn ions [67]. This behaviour is typically acompanied with an increase in μ, also observed Figs. 4 and 5 [68, 69].

Finally, the effect of thermally-induced and doping-induced structure variations on the fundamental absorption are traced by E_U and E_g. These are plotted in Fig. 6, for different annealing treatments and Tb concentrations. In this sense, E_U is used as an indirect measure of the lattice distortion. It can be noticed that larger lattice distortions, either induced by the presence of Tb ions or by thermal treatments in air, are correlated to a widening of the optical bandgap.

3.2. Electrical properties

All samples exhibited an ohmic behaviour when contacted by the four probes of the van der Pauw system. The effect of Tb incorporation and annealing treatments on the electrical resistivity ρ of ITO is depicted in Fig. 7. It is important to highlight that, contrary to the resistivity shown in Figs. 4 and 5, the values shown in Fig. 7 correspond to the whole ITO system, i.e. the two layers with different Drude parameters. As-grown Tb doped ITO exhibits its lowest ρ value for Tb concentrations around 0.5 at.%. Layers grown with active cooling and for Tb concentrations below 1.0 at.% have an oxygen concentration below 60 at.%. Thus, it is suggested, that in the as-grown state, a low Tb concentration favors the electrical properties of ITO thin films grown in this fashion. At higher Tb concentrations, lattice distortion plays an important role in quenching the electrical conductivity.

The dependence of the electrical resistivity of ITO and 2.3 at.% Tb doped ITO films with the annealing temperature is depicted also in Fig. 7. As annealing

treatments proceed, ρ decreases till 250 °C. For higher temperatures the resistivity increases again. This behaviour is in agreement with that reported for ITO thin films annealed in air [40, 58, 70, 71]. At first, annealing induces the formation of charged defects, improving the film conductivity. However, after annealing at higher temperatures in air, oxygen diffusion inside the layer quenches the number of charged vacancies [40, 71], and the formation of Sn-O and/or Tb-O complexes prevent the promotion of Sn^{4+} [58,67–71] A similar behaviour is observed in the case of Tb doped ITO films grown by sol-gel. [30].

3.3. Luminescence activation

It is well established that not all the Tb ions embedded in a host are optically active for emission and that these can be activated by post-deposition thermal treatments [20–22, 28]. The underlying mechanisms behind the thermally-induced activation and light emission enhancement are typically associated to: (i) the coordination of Tb ions with neighboring atoms in a non-centrosymmetric crystal field state, (ii) the thermally-induced promotion of energy transfer paths from the host to the REs after excitation [21, 22, 27], (iii) and the inhibition of back energy transfer processes. These establish a competition between the recombination in RE color centers and host-related radiative and non-radiative recombination centers [21, 72].

Here, the highest Tb-related light emission intensity is achieved after annealing at 550 °C. Figure 8 depicts the CL and PL spectra of 2.3 at.% Tb doped ITO under excitation by electrons at a 5 keV acceleration voltage and 325 nm light excitation, respectively. Characteristic Tb-related electronic transitions

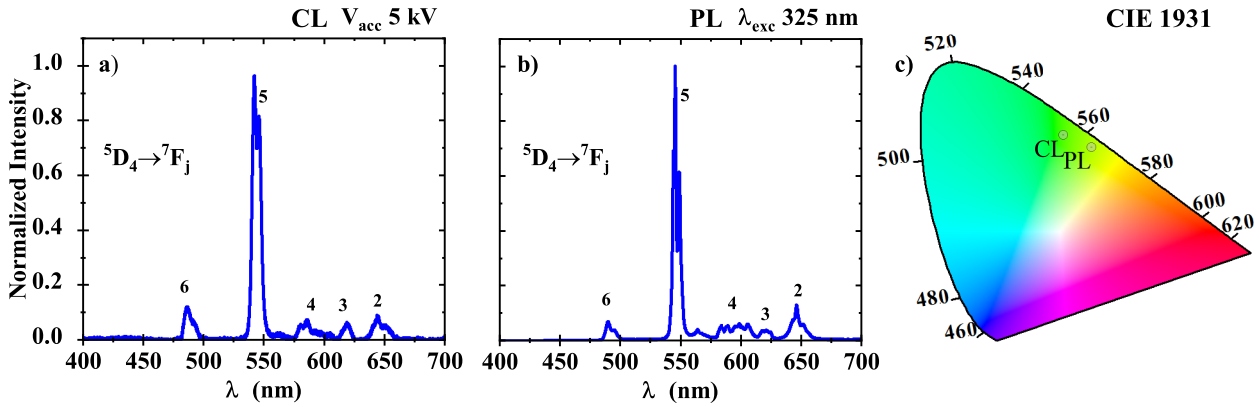

Figure 8: Room-temperature cathodoluminescence (a) and photoluminescence (b) spectra of a 2.3 at.% Tb doped ITO thin film after annealing at 550 °C in air for three hours. The corresponding coordinates in the CIE1931 color space are also depicted (c).

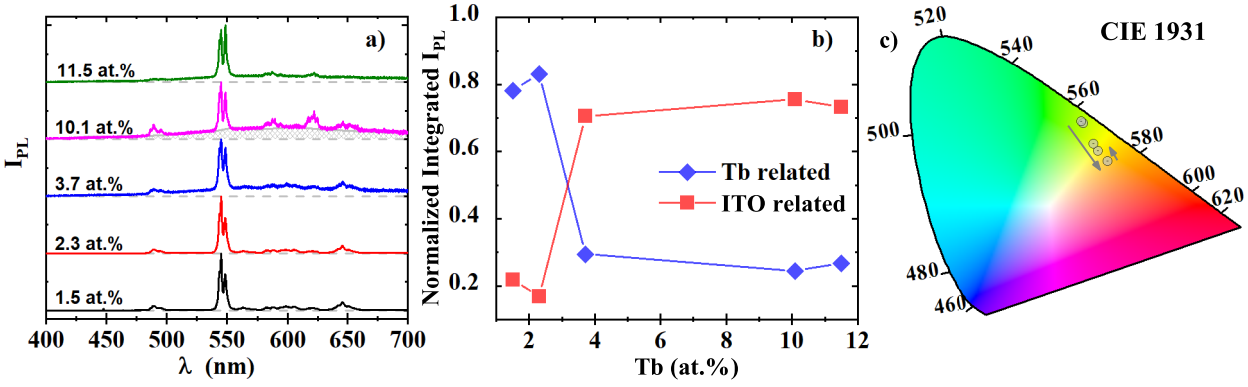

Figure 9: Room-temperature photoluminescence spectra of Tb doped ITO for distinct Tb concentrations. Note the increase in the background emission associated to host-related radiative recombination of ITO (a). Normalized integrated photoluminescence intensity for both the Tb-related and host-related emission (b). CIE1931 color space denoting the coordinates of the spectra for each Tb concentration (c).

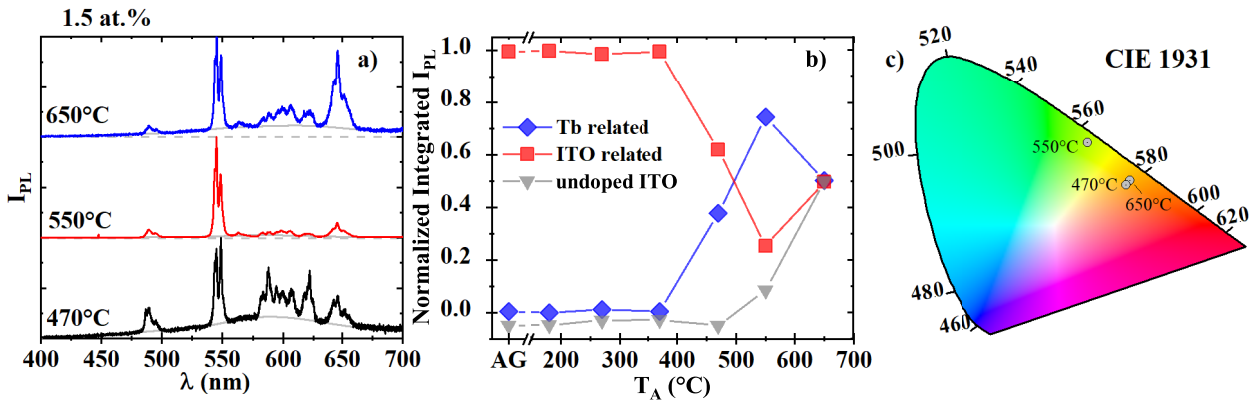

Figure 10: Room-temperature photoluminescence spectra of 1.5 at.% Tb doped ITO after three distinct annealing temperatures (a). Normalized integrated photoluminescence intensity for both the Tb-related and host-related emission. Additionally the light emission intensity evolution of an undoped ITO sample is included (b). The latter is shifted -0.5 for viewing reasons only. CIE1931 color space denoting the color shift of the Tb doped ITO spectra after each annealing treatment (c).

are identified. Additionally, the Commission International del'Eclarige (CIE1931) colorspace coordinates are also depicted in this figure for comparison purposes to track color differences.

The impact of the Tb concentration on the light emission intensity is depicted in Fig. 9. The concentration quenching effect can be noticed as the Tb-related light emission is quenched when increasing the RE concentration above a critical value. This is a consequence of the enhanced energy transfer probability between Tb ions due to their proximity. This enhancement increases the probability of back-transfer processes in which the recombination takes place in a localized state of the hos [73]. In this sense, whilst the Tb-related emission is quenched by the concentration quenching effect, host-related emission is enhanced.

In order to compare the variation of the Tb-related and host-related light emission intensities of distinct samples when varying the Tb content, the integrated emission is normalized versus the total integrated emission. That is, the integrated light emission intensity associated to the Tb ions is divided by the total integrated intensity. To do this, a background correction is performed. In particular the ITO host has a peak around 600 nm with a broad emission at room temperature. This was confirmed by measuring the PL spectrum of an undoped ITO sample. Naturally, the presence of the host emission in the spectra will have an impact in the visible color. The latter is depicted in CIE1931 colorspace in which a shift to a red color is observed when increasing the Tb amount due to the partaking of the host emission.

Samples doped with 1.5 at.% and 2.3 at.% Tb are the ones exhibiting the highest emission intensity. In order to try to avoid the impact of the concentration quenching effect, we focus on the sample doped with 1.5 at.% Tb. Figure 10 depicts the variation of the light emission spectra with annealing temperature. Almost no emission associated to Tb ions was registered for annealing temperatures below 470 °C. For these annealing temperatures, a strong host related background dominates the emission. After 550 °C annealing, the Tb emission reaches a maximum, with the $^5D_4 \rightarrow {}^7F_5$ electronic transition (∼545 nm), the most probable one. After 650 °C, host-related emission increases again. This is in agreement with an increased host emission observed in the undoped ITO sample treated at the same annealing conditions. This suggests a recombination competition between optically active Tb ions and host-related recombination centers.

Notably, after 650 °C annealing, the $^5D_4 \rightarrow {}^7F_2$ electronic transition (peak wavelength ∼650 nm) emission intensity is increased until it is almost as high as the $^5D_4 \rightarrow {}^7F_5$ (∼545 nm), shifting the apparent emission color to orange. Such unconventional variation of the 4f-shell electronic transition probabilities suggests a modification of the crystal field surrounding Tb ions, probably due to the presence of Tb ions in distinct crystalline sites with a non-centrosymmetric crystal field. In the present case, a crystallization after annealing treatments is observed, thus a variation of the crystal field is expected. Tb ions would replace In and/or Sn ions, see Fig. 1, thus distorting the lattice and occupying b and/or d sites in the ITO bixbyite crystalline structure. We believe that this might be the source behind the observed unconventional emission after the 650 °C annealing treatment, depicted in Fig. 10.

3.4. Thermal quenching

Temperature-dependent photoluminescence measurements were performed on the 1.5 at% Tb doped ITO sample annealed at 550 °C, in the temperature range from 83 K (−190 °C) to 533 K (260 °C). Figure 11 summarizes the variation of the emission spectra versus the sample temperature. At low temperatures, well defined Stark splitting lines can be observed, in agreement with the crystallization of the material after treatments at 550 °C.

The overall light emission intensity is quenched with increasing sample temperature, in contrast to the reported behaviour for Tb doped crystalline AlN [19] and amorphous AlN and SiN [22]. In fact, at temperatures above 373 K, the emission corresponds mainly to the host, as can be seen from the integrated normalized emission in Fig. 11.

An Arrhenius analysis is performed on the Tb-related integrated photoluminescence to assess the activation energies of the thermal quenching process. The integrated emission is modeled by means of a single (N = 1) and dual (N = 2) quenching channel Arrhenius equation [74, 75],

$$I(T) = \frac{I_0}{1 + \sum_{n=1}^{N} \exp\left(-\frac{\epsilon_n^b}{k_B}\left(\frac{1}{T} - \frac{1}{T_n}\right)\right)}. \quad (5)$$

Here k_B is the Boltzmann constant, T is the sample temperature, ϵ_n^b are the thermal activation energies, which can describe one or more possible thermal quenching channels. T_n are related to the relative ratios of the competing thermal quenching processes. The best fit parameters are summarized in Table 3.

Table 3: Best fitted parameters using equation (5) for single (N = 1) and dual (N = 2) thermal quenching processes. The reduced χ^2 is also shown for comparison purposes. Fits were performed in a logarithmic scale.

	Single	Dual
I_0	1.424E5 ± 8.5E3	1.57E5 ± 7.6E3
T_1 (K)	312.6 ± 4.6	290.6 ± 8.5
T_2 (K)	-	341.2 ± 10.6
ϵ_1^b (meV)	344.5 ± 14.9	152.0 ± 38.0
ϵ_2^b (meV)	-	453.9 ± 39.4
χ^2	0.036	0.014

3.5. Isovalent trap model

The observed Tb-related emission under 325 nm (3.81 eV) excitation could be the result of an overlap of direct resonant excitation of $4f$-shell electrons from the $^7F_6$ to the $^5D_1$ or $^5D_2$ enery levels, and host-assisted indirect excitation mechanisms. The former is considerably limited by the $4f$-shell cross section, whilst the latter can be attributed to distinct energy transfer processes. Indirect excitation mechanisms could be (i) Auger excitation of Tb ions near neutral dangling bonds [22, 29], (ii) dipole mediated resonant energy transfer from electron-hole ($e - h$) pairs [27], (iii) excitation by charge transfer from the host or a

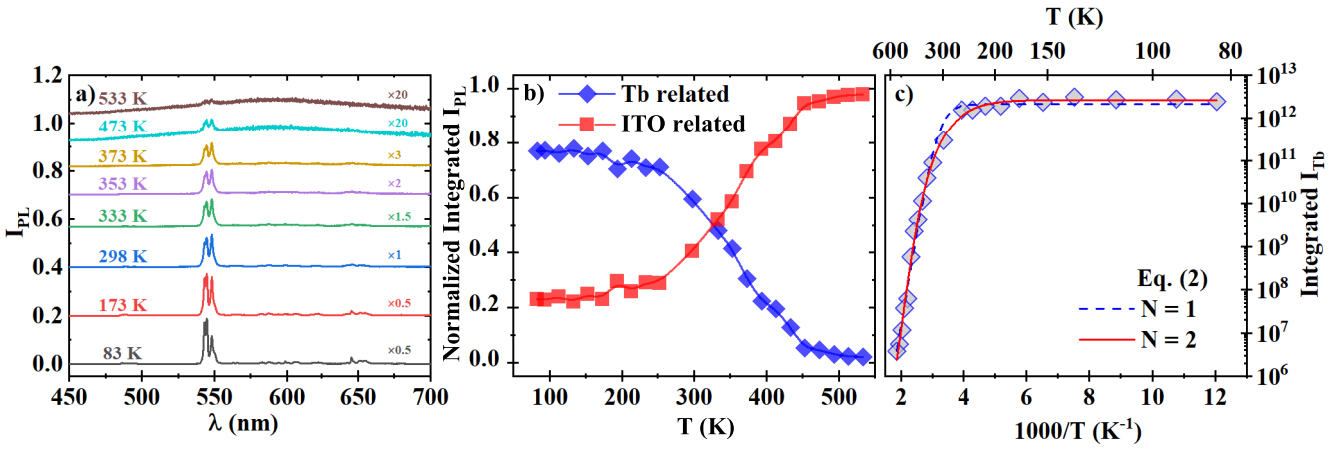

Figure 11: Photoluminescence spectra of 1.5 at.% Tb doped ITO after annealing at 550 °C at distinct sample temperatures. Here, the spectra at eight temperatures are depicted with vertical shifts and re-scaling for viewing reasons only (a). Normalized integrated photoluminescence intensity for both the Tb-related and host-related emission (b). Arrhenius plot of the Tb-related integrated photoluminescence (c). The fits correspond to equation (5) for one and two activation energies. The best fit is achieved when considering two activation energies.

metal (lanthanoid) ion with a different oxidation state [76–78] and (iv) excitation by energy transfer from the recombination of bound excitons to Tb ions [19].

Auger excitation (i) requires the proximity of Tb ions to neutral dangling bonds. Moreover, this mechanism is phonon assisted since a resonant energy transfer is not required and the excess energy can be taken by phonons. Here, no enhancement of the Tb-related light emission intensity is observed with the sample temperature, in contrast to the reported behaviour for Tb doped AlN and SiN [19, 22], suggesting this is not the most relevant mechanism for Tb doped ITO. On the other hand, dipole-mediated energy transfer (ii) is of long-range interaction. However, it must be resonant, thus limiting the probability of this mechanism in contrast to the other ones. Additionally, photoluminescence excitation spectra (not shown here) did not exhibit characteristic resonant bands when monitoring the $^5D_4 \rightarrow {}^7F_5$ emission band. Charge transfer (iii) requires a change in oxidation state and is typically accompanied with an additional broad emission band [77,79], which is not observed here. Therefore, here we attempt to model the excitation mechanism by means of (iv) energy transfer from recombination of bound excitons to Tb ions.

It is widely accepted that RE ions induce isovalent or isoelectronic cluster traps [19, 80–85]. There are some features that we can take into account for this, such as that the ionic radius of Tb^{3+} (0.923 Å) is bigger than that of In^{3+} (0.81 Å), which we assume it is substituting, and that Pauling's electronegativity of Tb^{3+} (1.2) is smaller than that of In^{3+} (1.78) [86,87]. Baldereschi [80] derived a simple electronegativity rule relating the pseudopotential depths for the outer s and p states, both of which are lower for heavier atoms. If the isovalent impurity is heavier than the host atom it replaces, the impurity is less electronegative than the replaced atom. This difference in electronegativity will create a short-range potential surrounding the impurity which is attractive to holes. Furthermore, the difference between the ionic radii of Tb^{3+} and In^{3+} generates distortion in the ITO lattice. There is an additional potential due to this distortion surrounding the Tb impurity that will increase the attraction of holes [19]. Therefore, the isovalent trap will be positively charged due to hole trapping and will afterwards attract an electron by long-range Coulomb interaction, creating a bound exciton. There would be no charge transfer ($h+$) neither from In^{3+} or Sn^{4+} lattice sites/interstitials nor from generated $e-h$ pairs to the Tb^{3+} ion to form Tb^{4+}, which is known to be a non-luminescent center and could also act as a Tb^{3+} luminescence killer [88].

The binding energies of a hole bound to an isovalent cluster trap were calculated using both the spherical potential-well (SPW) and the Koster-Slater (KS) models. Different from the calculation done by Lozykowski [19], both fitted energies were used to calculate the parameters corresponding to each model, assuming the lowest energy for $n = 1$ (singlet) and the largest for $n = 2$ (dimer), n being the number of RE ions forming the cluster. Subsequently, these calculated parameters were employed to estimate the corresponding energies for larger clusters, $n \geq 3$.

In the SPW model, the binding of a hole trapped to a RE-cluster isovalent trap can be described by a three-dimensional spherical potential-well with an effective depth $-V_0$ and radius ρ_1. In the case of clusters with $n > 1$, the model assumes the cluster to contribute a potential well with the same depth $-V_0$ and an effectively enlarged radius, ${}^{\text{eff}}\rho_n = n^{1/3}\rho_1$. The binding energy of a hole bound to a n-cluster is given by [46]

$$\epsilon_{\text{n}}^{\text{b}} = \frac{\hbar^2 \beta_{\text{n}}^2}{2m^* \, {}^{\text{eff}}\rho_n^2}, \tag{6}$$

with

$$\beta_{\text{n}} = -\left(\frac{2m^* V_0 \, {}^{\text{eff}}\rho_n^2}{\hbar^2} - \beta_{\text{n}}^2\right)^{1/2} \times \cot\left[\left(\frac{2m^* V_0 \, {}^{\text{eff}}\rho_n^2}{\hbar^2} - \beta_{\text{n}}^2\right)^{1/2}\right]$$

and

$${}^{\text{eff}}\rho_{\text{n}} = n^{1/3}\rho_1.$$

Here m^* is the average effective mass. Baldereschi [80] suggested that for covalent materials m^* is 0.9 m_0 and for III-V compounds it 1.2 m_0, m_0 being the free electron mass at rest. Since ITO has a more covalent than ionic bonding structure, we make the assumption that m^* is simply equal to m_0. The parameters calculated with this model are shown in Table 4.

Table 4: SPW and KS parameters obtained from Eqs. 6 and 8 using the activation energies derived from the thermal quenching behaviour of the luminescence.

SPW	ρ_1 (nm)	0.29 ± 0.02
	V_0 (eV)	1.67 ± 0.04
KS	T (eV)	5.08 ± 0.35
	J (eV)	1.79 ± 0.03

The obtained small radius corroborates our assumption of a strong localization of the effective impurity potential. Oxygen atoms in the cubic bixbyite structure of ITO have four different bond lengths with respect to the b- or d- sites that the

Tb ion would occupy: 2.13 Å, 2.18 Å, 2.19 Å and 2.23 Å [89]. Furthermore, it has been suggested that the Tb-O bond length is 2.35-2.57 Å in polymers [90], mononuclear complexes [91] and simulations [92]. Hence, the calculated effective radius of influence for this short-range impurity potential is relatively close to these Tb-O bond length values.

For the KS model, a one-band one-site tight-binding approximation is employed, assuming a Hubbard density of states [47]. This approximation requires only two parameters, i.e. the matrix element of the impurity potential J, and the effective valence band width of the host T, see Eq. (7) for $n = 1$ and Eq. (8) for $n > 1$.

$$\epsilon_1^{\mathrm{b}} = J\left(1 - \frac{T}{4J}\right)^2 \tag{7}$$

$$\epsilon_{\mathrm{n}}^{\mathrm{b}} = \frac{1}{2}\left[J - \frac{2n-1}{2n-2}T + \left(J + \frac{T}{2n-2}\right) \times \left(1 + \frac{n-1}{2}\frac{T}{J}\right)^{1/2}\right] \tag{8}$$

The hole binding energies derived from these equations are approximately equal to binding energies of excitons bound to the RE isovalent impurity, with respect to the free exciton energy [47, 81]. Eqs. (7) and (8) were used to calculate J and T values, with the experimental binding energies obtained from the thermal quenching analysis. The uppermost valence band width for ITO is around 6 eV, as estimated by both simulated [89,93] and experimental [94] methods. Our calculated value for T, given in Table 4, represents a good approximation.

Figure 12 depicts the exciton binding energies for distinct cluster sizes obtained from the SPW and KS models by using the previously determined thermal quenching activation energies. This is assuming the latter activation energies are the necessary energy to break bound excitons and/or release trapped holes, and thus inhibit the RE excitation. Further research is necessary to confirm this range of values experimentally for this and other similar materials.

4. Summary and conclusions

In this work, we have effectively embedded Tb ions in ITO thin films by co-sputtering. Samples were grown by actively cooling the substrates during the deposition process in order to limit grain sizes and induce an amorphous phase to subsequently allow the thermally induced RE activation by means of post-deposition annealing treatments. This strategy proved useful since Tb-related light emission was achieved

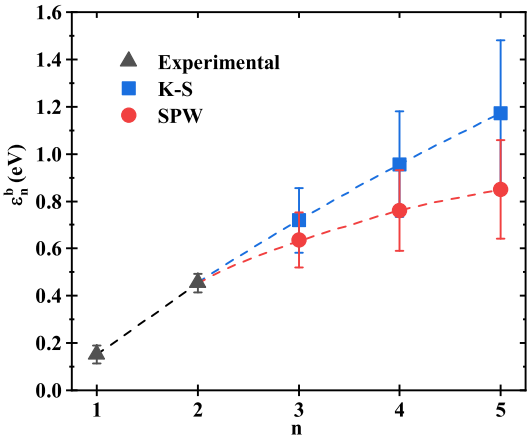

Figure 12: Exciton binding energies calculated by the SPW and KS aproaches for different cluster sizes. Experimental values correspond to those determined by the thermal quenching effect. Dashed lines are a guide to the eye.

for annealing temperatures above 400 °C. Under these conditions, electrical resistivity measurements showed that Tb doped ITO thin films exhibit a higher resistivity than that of pure ITO for concentrations above 1.0 at.%, whilst a lower resistivity is observed for smaller Tb concentrations. On the other hand, the observed behaviour of the Tb doped ITO resistivity versus annealing temperature is similar to that of the non-doped ITO film resembling the behaviour reported previously in the literature [58, 71]. The behaviour of the charged carrier density depicted in Fig. 4 suggest that oxygen diffusion occurs at temperatures higher than 250 °C, whilst ITO crystallization takes place at lower temperatures [40], both processes affecting the electronic properties of the material.

The optical absorption edge is strongly affected by the Tb concentration. This is probably due to the Tb affinity to oxidation, which enhances the formation of Tb-O complexes, and to the induced lattice distortion increasing disorder related localized states. The effect of thermal treatments and Tb concentration in the structure is traced down by the Urbach energy and optical bandgap. Both increase with annealing temperature and Tb concentration, suggesting, at least for samples with Tb concentrations below 1.0 at.%, an increase in the charge carrier density by charged defect states, such as oxygen vacancies, that may be responsible for the observed reduction in the electrical resistivity at this doping regime and for samples grown in this fashion.

Annealing treatments in Tb doped non-degenerate wide bandgap semiconductors usually do not suggest an optimal Tb ion activation temperature [21, 29, 95, 96]. In these hosts, predominant energy transfer

processes change with annealing treatments at high temperatures due to modifications in their structure, although at these temperatures more ions could be effectively activated [96]. In contrast to this behaviour, here the light emission intensity versus annealing temperature suggests that there is an optimum annealing temperature for which Tb ions are effectively activated to be excited. This might be related to a competition between the energy transfer to Tb ions and host related luminescent centers. Moreover, after annealing at 650 °C, the $^5D_4 \rightarrow {}^7F_2$ Tb electronic transition is considerably enhanced, shifting the emission color to red. This unexpected enhancement might be attributed to a particular crystal field surrounding Tb ions, for instance in either b- or d- sites of the crystalline lattice.

Finally, temperature-dependent photoluminescence measurements on the 1.5 at.% Tb doped ITO showed a continuous decrease of the Tb-related light emission intensity. Two activation energies were determined from the luminescence thermal quenching. By assuming that the main Tb excitation mechanism is due to the energy transfer from recombination of bound excitons to RE isovalent traps, these energies were used to determine the SPW and KS models parameters. The calculated singlet effective interaction radius (ρ_1) is slightly larger and in agreement with the Tb-O bond length, whilst the effective valence band width (T) is in agreement with values reported in the literature [89,93,94]. We believe that these results will open a pathway to enhance the light emission intensity of RE doped TCOs without compromising considerably their transparency and electrical conductivity.

5. Acknowledgments

This research was funded by the Peruvian National Fund for Scientific and Technologial Development (FONDECYT), grant no. 179-2020-FONDECYT, and was supported by the Research Management Office (DGI) of the Pontificia Universidad Católica del Perú (PUCP), grant no. 2019-3-0041/702 and the Office of Naval Research, grant no. N62909-21-1-2034. The authors acknowledge the CITE and CAM laboratories of the PUCP for supporting the development of this work. Further support for travel expenses has been provided by the DAAD-CONCYTEC grants no 423-2019 and 57508544.

References

[1] Bai G, Yuan S, Zhao Y, Yang Z, Choi S Y, Chai Y, Yu S F, Lau S P and Hao J 2016 *Adv. Mater.* **28** 7472–7477
[2] Yao N, Huang J, Fu K, Deng X, Ding M and Xu X 2016 *RSC Adv.* **6** 17546–17559
[3] Xing P, Chen G F R, Zhao X, Ng D K T, Tan M C and Tan D T H 2017 *Sci. Rep.* **7** 9101
[4] Kenyon A 2002 *Prog. Quantum Electron.* **26** 225–284
[5] Lee D S and Steckl A J 2003 *Appl. Phys. Lett.* **83** 2094–2096
[6] Li L, Wang S, Mu G, Yin X and Yi L 2017 *Sci. Rep.* **7** 42479
[7] Kränkel C, Marzahl D T, Moglia F, Huber G and Metz P W 2016 *Laser Photon. Rev.* **10** 548–568
[8] Nemova G and Kashyap R 2014 *J. Opt. Soc. Am. B* **31** 340
[9] Scoca D, Morales M, Merlo R, Alvarez F and Zanatta A R 2015 *J. Appl. Phys.* **117** 205304
[10] Zanatta A R, Scoca D and Alvarez F 2017 *Sci. Rep.* **7** 14113
[11] Getz M N, Nilsen O and Hansen P A 2019 *Sci. Rep.* **9** 10247
[12] Geng D, Cabello-Olmo E, Lozano G and Míguez H 2018 *Mater. Horizons* **5** 661–667
[13] Gallo I B, Braud A and Zanatta A R 2013 *Opt. Express* **21** 28394
[14] Zhang F, Deng Y, Shi Y, Zhang R and Zhao D 2010 *J. Mater. Chem.* **20** 3895
[15] Dumont L, Cardin J, Labbé C, Frilay C, Anglade P M, Yu I S, Vallet M, Benzo P, Carrada M, Stiévenard D, Merabet H and Gourbilleau F 2019 *Prog. Photovoltaics Res. Appl.* **27** 152–162
[16] Ho W J, Liu J J, Lin Z X and Shiao H P 2019 *Nanomaterials* **9** 1518
[17] Dumont L, Benzo P, Cardin J, Yu I S, Labbé C, Marie P, Dufour C, Zatryb G, Podhorodecki A and Gourbilleau F 2017 *Sol. Energy Mater. Sol. Cells* **169** 132–144
[18] Weingärtner R, Erlenbach O, Winnacker A, Welte A, Brauer I, Mendel H, Strunk H, Ribeiro C and Zanatta A 2006 *Opt. Mater. (Amst).* **28** 790–793
[19] Lozykowski H J and Jadwisienczak W M 2007 *Phys. status solidi* **244** 2109–2126
[20] Zanatta A R 2009 *J. Phys. D. Appl. Phys.* **42** 025109
[21] Guerra J A, De Zela F, Tucto K, Montañez L, Töfflinger J A, Winnacker A and Weingärtner R 2016 *J. Phys. D. Appl. Phys.* **49** 375104
[22] Guerra J A, Montañez L, Winnacker A, De Zela F and Weingärtner R 2015 *Phys. status solidi* **12** 1183–1186
[23] Zanatta A R 2012 *J. Appl. Phys.* **111** 123105
[24] Zanatta A R 2016 *J. Appl. Phys.* **119** 145302
[25] Guerra J A, Benz F, Zanatta A R, Strunk H P, Winnacker A and Weingärtner R 2013 *Phys. status solidi* **10** 68–71
[26] Sunde T O L, Lindgren M, Mason T O, Einarsrud M and Grande T 2014 *Dalton Trans.* **43** 9620–9632
[27] Janotta A, Schmidt M, Janssen R, Stutzmann M and Buchal C 2003 *Physical Review B* **68** 165207
[28] Tucto K Y, Aponte W, Dulanto J A, Töfflinger J A, Guerra J A and Grieseler R 2019 *Appl. Opt.* **58** 3097
[29] Bosco G B, Khatami Z, Wojcik J, Mascher P and Tessler L R 2018 *J. Lumin.* **202** 327–331
[30] Skjærvø S H 2013 *Terbium Doped ITO Thin Films Prepared by an Aqueous Sol-Gel Method* Master thesis Norwegian University of Science and Technology
[31] Anand V, Sakthivelu A, Kumar K D A, Valanarasu S, Ganesh V, Shkir M, AlFaify S and Algarni H 2018 *J. Sol-Gel Sci. Technol.* **86** 293–304
[32] Anand V, Sakthivelu A, Kumar K D A, Valanarasu S, Kathalingam A, Ganesh V, Shkir M, AlFaify S and Yahia I 2018 *Ceram. Int.* **44** 6730–6738
[33] Ziani A, Davesnne C, Labbé C, Cardin J, Marie P, Frilay C, Boudin S and Portier X 2014 *Thin Solid Films* **553** 52–57
[34] Miranda S, Peres M, Monteiro T, Alves E, Sun H, Geruschke T, Vianden R and Lorenz K 2011 *Opt. Mater.* **33** 1139–1142
[35] Penilla E H, Kodera Y and Garay J E 2013 *Adv. Funct. Mater.* **23** 6036–6043
[36] Chen L C, Tien C H and Liao W C 2011 *J. Phys. D. Appl. Phys.* **44** 165101
[37] Ghosh S, Das K, Sinha G, Lahtinen J and De S K 2013 *J. Mater. Chem. C* **1** 5557

[38] Elhouichet H, Othmen W B H and Dabboussi S 2020 *Silicon* **12** 715–722
[39] Singh L P, Singh N P and Srivastava S K 2015 *Dalt. Trans.* **44** 6457–6465
[40] Neubert T, Neumann F, Schiffmann K, Willich P and Hangleiter A 2006 *Thin Solid Films* **513** 319–324
[41] ASTM E1508-12a(2019) Standard Guide for Quantitative Analysis by Energy-Dispersive Spectroscopy Standard ASTM International
[42] Tejada A, Montañez L, Torres C, Llontop P, Flores L, De Zela F, Winnacker A and Guerra J A 2019 *Appl. Opt.* **58** 9585
[43] Synowicki R 1998 *Thin Solid Films* **313-314** 394–397
[44] Uprety P, Junda M M, Salmon H and Podraza N J 2018 *J. Phys. D. Appl. Phys.* **51** 295302
[45] Yu P Y and Cardona M 2010 *Fundamentals of Semiconductors* (Springer-Verlag Berlin Heidelberg)
[46] Goede O, Heimbrodt W and Müller R 1981 *Phys. status solidi* **105** 543–550
[47] Hennig D, Goede O and Heimbrodt W 1982 *Phys. status solidi* **113** K163–K167
[48] Tien C L, Lin H Y, Chang C K and Tang C J 2018 *Adv. Condens. Matter Phys.* **2018** 1–6
[49] Guerra J A, Tejada A, Töfflinger J A, Grieseler R and Korte L 2019 *J. Phys. D. Appl. Phys.* **52** 105303
[50] Guerra J A, Angulo J R, Gomez S, Llamoza J, Montañez L M, Tejada A, Töfflinger J A, Winnacker A and Weingärtner R 2016 *J. Phys. D. Appl. Phys.* **49** 195102
[51] Guerra J A, Tejada A, Korte L, Kegelmann L, Töfflinger J A, Albrecht S, Rech B and Weingärtner R 2017 *J. Appl. Phys.* **121** 173104
[52] Tejada A, Braunger S, Korte L, Albrecht S, Rech B and Guerra J A 2018 *J. Appl. Phys.* **123** 175302
[53] Kim H, Gilmore C M, Piqué A, Horwitz J S, Mattoussi H, Murata H, Kafafi Z H and Chrisey D B 1999 *J. Appl. Phys.* **86** 6451–6461
[54] Singh N S, Singh S D and Meetei S D 2014 *Chin. Phys. B* **23** 058104
[55] Shkir M, Chandekar K V, Alshahrani T, Kumar A and AlFaify S 2020 *J Mater Res* **35** 2664–2675
[56] Chetri P, Saikia B and Choudhury A 2013 *J. Appl. Phys.* **113** 233514
[57] Paine D C, Whitson T, Janiac D, Beresford R, Yang C O and Lewis B 1999 *J. Appl. Phys.* **85** 8445–8450
[58] Takayama S, Sugawara T, Tanaka A and Himuro T 2003 *J. Vac. Sci. Technol. A Vacuum, Surfaces, Film.* **21** 1351–1354
[59] Dhere R, Gessert T, Schilling L, Nelson A, Jones K, Aharoni H and Coutts T 1987 *Sol. Cells* **21** 281–290
[60] Gessert T A, Williamson D L, Coutts T J, Nelson A J, Jones K M, Dhere R G, Aharoni H and Zurcher P 1987 *J. Vac. Sci. Technol. A Vacuum, Surfaces, Film.* **5** 1314–1315
[61] Jellison G E and Modine F A 1996 *Appl. Phys. Lett.* **69** 371–373
[62] Jung Y S 2004 *Thin Solid Films* **467** 36–42
[63] Lee H C and Ok Park O 2006 *Vacuum* **80** 880–887
[64] Kim S S, Choi S Y, Park C G and Jin H W 1999 *Thin Solid Films* **347** 155–160
[65] Kaiser N 2002 *Appl. Opt.* **41** 3053
[66] Gupta L, Mansingh A and Srivastava P 1989 *Thin Solid Films* **176** 33–44
[67] Furubayashi Y, Maehara M and Yamamoto T 2019 *ACS Appl. Electron. Mater.* **1** 1545–1551
[68] Han H, Mayer J W and Alford T L 2006 *J. Appl. Phys.* **99** 123711
[69] Han H, Mayer J W and Alford T L 2006 *J. Appl. Phys.* **100** 083715
[70] Chen Y, Jiang H, Jiang S, Liu X, Zhang W and Zhang Q 2014 *Acta Metall. Sin. (English Lett.)* **27** 368–372
[71] Higuchi M, Uekusa S, Nakano R and Yokogawa K 1994 *Jpn. J. Appl. Phys.* **33** 302–306
[72] Benz F, Guerra J A, Weng Y, Weingärtner R and Strunk H P 2013 *Phys. status solidi* **10** 109–112
[73] Layek A, Banerjee S, Manna B and Chowdhury A 2016 *RSC Adv.* **6** 35892–35900
[74] Buyanova I A, Izadifard M, Chen W M, Polimeni A, Capizzi M, Xin H P and Tu C W 2003 *Appl. Phys. Lett.* **82** 3662–3664
[75] Lambkin J D, Considine L, Walsh S, O'Connor G M, McDonagh C J and Glynn T J 1994 *Appl. Phys. Lett.* **65** 73–75
[76] Dorenbos P and van der Kolk E 2008 *Optical Materials* **30** 1052–1057
[77] Joos J J, Van der Heggen D, Martin L I D J, Amidani L, Smet P F, Barandiarán Z and Seijo L 2020 *Nat. Commun.* **11** 3647
[78] dos Santos J F M, Terra I A A, Astrath N G C, Guimarães F B, Baesso M L, Nunes L A O and Catunda T 2015 *J. Appl. Phys.* **117** 053102
[79] Wybourne B G and Meggers W F 1965 *Phys. Today* **18** 70–72
[80] Baldereschi A 1973 *J. Lumin.* **7** 79–91
[81] Goede O and Hennig D 1983 *Phys. status solidi* **119** 261–268
[82] Lozykowski H J 1993 *Phys. Rev. B* **48** 17758–17769
[83] Shin J H, van den Hoven G N and Polman A 1995 *Appl. Phys. Lett.* **67** 377–379
[84] Nepal N, Zavada J M, Lee D S, Steckl A J, Sedhain A, Lin J Y and Jiang H X 2009 *Appl. Phys. Lett.* **94** 111103
[85] Wang J, Koizumi A, Fujiwara Y and Jadwisienczak W M 2016 *J. Electron. Mater.* **45** 6355–6362
[86] González G B, Cohen J B, Hwang J H, Mason T O, Hodges J P and Jorgensen J D 2001 *J. Appl. Phys.* **89** 2550–2555
[87] Gupta C and Krishnamurthy N 2004 *Extractive Metallurgy of Rare Earths* (Boca Raton: CRC Press)
[88] Kaszewski J, Witkowski B S, Wachnicki Ł, Przybylińska H, Kozankiewicz B, Mijowska E and Godlewski M 2016 *J. Rare Earths* **34** 774–781
[89] Tripathi M N, Shida K, Sahara R, Mizuseki H and Kawazoe Y 2012 *J. Appl. Phys.* **111** 103110
[90] Kittipong C, Khemthong P, Kielar F and Zhou Y 2016 *Acta Crystallogr. Sect. E Crystallogr. Commun.* **72** 87–91
[91] Gregório T, Giese S O K, Nunes G G, Soares J F and Hughes D L 2017 *Acta Crystallogr. Sect. E Crystallogr. Commun.* **73** 278–285
[92] Lu J B, Cantu D C, Nguyen M T, Li J, Glezakou V A and Rousseau R 2019 *J. Chem. Theory Comput.* **15** 5987–5997
[93] Wan D, Chen P, Liang J, Li S and Huang F 2011 *ACS Appl. Mater. Interfaces* **3** 4751–4755
[94] Körber C, Krishnakumar V, Klein A, Panaccione G, Torelli P, Walsh A, Da Silva J L F, Wei S H, Egdell R G and Payne D J 2010 *Physical Review B* **81** 165207
[95] Zhou J, Song D, Zhao H, Pan X, Zhang Z, Mao Y, Fu Y, Wang T and Xie E 2015 *J. Lumin.* **157** 119–125
[96] Wahl U, Alves E, Lorenz K, Correia J, Monteiro T, De Vries B, Vantomme A and Vianden R 2003 *Mater. Sci. Eng. B* **105** 132–140